Bayesian approach to the tomographic problem with constraints from geodynamic modeling: Application to a synthetic subduction zone

John Keith Magali, Thomas Bodin

▶ **To cite this version:**

John Keith Magali, Thomas Bodin. Bayesian approach to the tomographic problem with constraints from geodynamic modeling: Application to a synthetic subduction zone. Seismica, 2022, 1, 10.26443/seismica.v1i1.201 . hal-04313028

HAL Id: hal-04313028
https://cnrs.hal.science/hal-04313028

Submitted on 28 Nov 2023

HAL is a multi-disciplinary open access archive for the deposit and dissemination of scientific research documents, whether they are published or not. The documents may come from teaching and research institutions in France or abroad, or from public or private research centers.

L'archive ouverte pluridisciplinaire **HAL**, est destinée au dépôt et à la diffusion de documents scientifiques de niveau recherche, publiés ou non, émanant des établissements d'enseignement et de recherche français ou étrangers, des laboratoires publics ou privés.

doi:10.26443/seismica.v1i1.201

A Bayesian Approach to the Tomographic Problem with Constraints from Geodynamic Modeling: Application to a Synthetic Subduction Zone

John Keith Magali * [1,2], **Thomas Bodin** [2]

[1]Université de Lille, CNRS. INRA, ENSCL, UMR 8207 - UMET - Unité Matériaux et Transformations, 59000 Lille, France, [2]Univ Lyon, Univ Lyon 1, ENSL, UJM-Saint-Etienne, CNRS, LGL-TPE, F-69622, Villeurbanne, France

Author contributions: *Conceptualization*: JKM, TB. *Methodology*: JKM, TB. *Software*: JKM. *Validation*: JKM. *Formal Analysis*: JKM. *Investigation*: JKM. *Resources*: TB. *Writing - original draft*: JKM. *Writing - Review & Editing*: TB. *Visualization*: JKM. *Supervision*: TB. *Funding acquisition*: TB.

Abstract Geodynamic tomography, an imaging technique that incorporates constraints from geodynamics and mineral physics to restrict the potential number of candidate seismic models down to a subset consistent with geodynamic predictions, is applied to a thermal subduction model. The goal is to test its ability to recover structures harboring complex deformation patterns. The subduction zone is parameterized in terms of four unknown parameters that define its thermal structure: slab length L, thickness R, temperature T_c, and dip angle θ. A temperature-dependent viscosity is prescribed with an activation coefficient E controlling the sensitivity. Using the full forward approach to geodynamic tomography, we generate anisotropic surface wave dispersion measurements as synthetic data. We retrieve the five unknown parameters by inverting the synthetics corrupted with random uncorrelated noise. The final output is an ensemble of models of L, R, θ, T_c, and E cast in a posterior probability distribution with their uncertainty limits. Results show that the parameters are tightly constrained with the apparent existence of a single misfit minima in each of them, implying the implicit retrieval of the complete patterns of upper mantle deformation, and the 21-independent coefficients defining elastic anisotropy. Each model realization, however, fails to swarm around its true value. Such results are attributed to the inability of the surrogate model to accurately replicate the correct forward model for computing anisotropy due to the complexity of the deformation patterns considered. Nevertheless, this proof of concept shows a self-consistent method that incorporates mantle flow modeling in a seismic inversion scheme.

Production Editor: Gareth Funning
Handling Editor: Paula Koelemeijer
Copy & Layout Editor: Kirsty Bayliss

Received: July 12, 2022
Accepted: November 21, 2022
Published: December 12, 2022

Non-technical summary Seismic tomography is an active area of research in seismology that primarily deals with the imaging of the Earth interior. Here, seismic data are used to recover the heterogeneous structure of the Earth at a given resolution in a process known as inversion. However, seismic inversion methods have to be constantly improved to accurately map these heterogeneities in order to correctly interpret them in terms of recent deformation mechanisms within the Earth. We introduce geodynamic tomography; a new imaging technique that infers the present-day temperature and mantle flow patterns from the inversion of surface wave measurements. We demonstrate this method in a subduction zone setting (an earthquake prone area where materials making up a tectonic plate are recycled into the mantle) by recovering some properties that define its thermal structure: length, thickness, angle of subduction, and slab core temperature.

1 Introduction

Backed by numerous seismic tomography studies at the global (e.g. Montagner and Tanimoto, 1991; Panning and Romanowicz, 2006) and regional scale (e.g. Montagner and Jobert, 1988; Debayle and Kennett, 2000), the Earth's upper mantle exhibits large scale anisotropy which have been mainly attributed to the development of the crystallographic preferred orientation (CPO) of olivine aggregates as they get advected by mantle flow (see Long and Becker, 2010, for a comprehensive review).

In practice, observations of seismic anisotropy rely on the simplification of the full elastic tensor (*i.e.* a fourth rank tensor of elasticity with 21 independent coefficients) because seismic waves are only sensitive to a limited number of coefficients. Tilted transverse isotropy (TTI) is one of the most convenient ways to simplify the elastic tensor, if not the most. In such a symmetry, the elastic constants can be defined by the five Love parameters A_0, C_0, F_0, L_0, and N_0, and two angles that define the dip and the azimuth, respectively, of the symmetry axis (Love, 1927). Particularly for $S-$wave anisotropy, further simplifications can be defined to reduce the model dimensionality. On one end, we have horizontal transverse isotropy (HTI) where the axis of symmetry is horizontal. Also called azimuthal anisotropy, here $S-$wave speeds vary with propagation direction. On the other, we have vertical transverse isotropy (VTI) where the axis of symme-

*Corresponding author: jkvmagali@gmail.com

try is vertical as a consequence of azimuthal averaging. Also called $S-$wave radial anisotropy, this property causes shear wave speeds to vary with polarization orientation instead. In theory, constraining the tilt of anisotropy is possible (Montagner and Nataf, 1988), and in practice has already been implemented in the regional scale (Xie et al., 2015, 2017). However due to sparse azimuthal sampling, non-uniqueness of the solutions, and finite frequency effects brought by tilted layers, this may make its implementation discouraging.

Surface waves provide unique constraints to large scale anisotropy in the upper mantle. $S-$wave radial anisotropy, for instance, can be recovered through joint inversions of Love and Rayleigh wave velocities (Babuska and Cara, 1991). Likewise, azimuthal anisotropy can be effectively constrained by adding the azimuthal terms of surface wave velocities in the data vector(Smith and Dahlen, 1973). Similar to what was previously mentioned, surface waves are effectively sensitive to 9 depth functions of the elastic constants when poor azimuthal coverage is taken into account: 5 for radial anisotropy given by the previously mentioned Love parameters; and 4 for azimuthal anisotropy given by G_c, G_s, and B_c, B_s, whose kernels are identical to that of $S-$ and $P-$waves, respectively (Montagner and Nataf, 1986).By itself however, 9 unknown parameters are still an excessive amount to be inverted for, and still can be difficult to resolve. Because of this, velocity and anisotropy ratios are imposed ad-hoc for regularization (Obrebski et al., 2010, 2011) which may potentially bias the results. Moreover due to its limited sensitivity to the elastic tensor, we are left with a rudimentary understanding of mantle deformation processes when relying on tomographic images alone. Thus, complete knowledge of the full elastic tensor is imperative to capture the complete patterns of upper mantle deformation.

2 Background: Geodynamic tomography

Geodynamic tomography, as reported in Magali et al. (2021b), is a novel approach to the tomographic problem whose two key features are the reduction of the number of unknowns and the removal of symmetry relations to the elastic tensor through the incorporation of geodynamic and petrological constraints. Due to its high non-linearity , the solutions to the tomographic problem are appraised based on a Bayesian probability framework (i.e. the posterior).

Under Bayesian inference, geodynamic tomography may not be a conventional inverse problem per se because it proposes a set of unknown parameters, computes the forward model, and compares the estimated to the observed data thousands of times. The efficient search for plausible solutions is carried out through a Markov chain Monte Carlo (McMC) algorithm. Here, McMC ultimately tends to sample a restricted area of high probability density and operates according to a random-walk behavior. At this point, the chain is said to be converged; meaning that the target posterior has been successfully approximated.

As of its current implementation, the method only inverts local surface wave phase velocity dispersion curves and their azimuthal variations for the retrieval of the thermal structure. In practice, dispersion curves can be obtained by stacking 2-D surface wave velocity maps with period, and then recovering a plot of phase velocities versus period at a given geographical location (e.g. Nakanishi and Anderson, 1983; Romanowicz, 2002). As such, it is under the assumption of geodynamic tomography that dispersion curves (which are also a product of inversion) are readily available. Although there have been a growing number of studies that implement probabilistic approaches to invert for the thermal (and chemical) structure from multiple data types, which include surface wave dispersion measurements such as in Afonso et al. (2013b,a), and Bissig et al. (2021), geodynamic tomography incorporates mantle flow modeling followed by texture evolution computations to constrain strain-induced seismic anisotropy, and potentially the medium rheology.

Given a temperature field and assuming a strictly temperature-dependent viscosity, mantle flow models are obtained using an instantaneous approach. In this approach, it is not necessary to include the conservation of energy in solving the equations of viscous fluid flow. As a result, a steady-state assumption in the flow is implied when tracing flow streamlines backwards in time. Instantaneous models with a steady-state assumption may be valid if we interpret the temperature field as its present-day structure, and assume that the timescale for the development of strain-induced anisotropy in mantle minerals is much faster than the variations of mantle flow velocities with time. Because of this, geodynamic tomography is not suitable to invert for the evolution history of the temperature field.

For each flow line traced, undeformed aggregates composed of a discrete number of crystals are placed at a position in the streamline corresponding to the first time step. Texture evolution modeling is then implemented to track the strain evolution of the aggregates along the streamline. The texture evolution model currently implemented in our forward problem uses an 'average field' formalism (Kaminski et al., 2004). Here, unlike finite-element approaches where the aggregate is explicitly deemed as a spatially extended body, it is not necessary to keep track of the interaction among crystals. Instead, the crystals within the aggregate are finite and are treated as a collective entity in a homogeneously isotropic medium whose properties are the weighted mean of the properties of each crystal. The output of the texture evolution model is the full elastic tensor. This tensor can be decomposed into much simpler forms for easier interpretation. For instance, it can be decomposed into a VTI medium using the method of Montagner and Nataf (1986) to obtain radial anisotropies in $P-$ and $S-$waves.

Magali et al. (2021b) highlights the success of geodynamic tomography in the recovery of the complete patterns of upper mantle deformation from anisotropic surface wave measurements in the most simple cases (i.e. instantaneous flow induced by spherical tempera-

ture anomalies). This paper explores the ability of the method to capture more complex deformation patterns in the guise of a 3-D instantaneous flow across the upper mantle induced by subduction, and so directly serves as an extension to Magali et al. (2021b). To do so, we model thermal subduction by applying a continuous parameterization of the subducting slab in terms of hyperbolic tangent basis functions on top of a background temperature field. The basis function depends on four parameters which would be treated as unknowns: (1) slab length L, (2) slab thickness R, (3) dip angle θ, and (4) slab temperature T_c. For the medium rheology, we employ a temperature-dependent viscosity controlled by a scalar parameter called the activation coefficient, E; although it is acknowledged that a realistic parameterization involves the implementation of non-linear rheologies relevant to upper mantle conditions (Karato and Wu, 1993). We implement geodynamic tomography to retrieve these five unknown parameters that define the thermal and rheological structure of a synthetic subduction zone. The method is tested to synthetic data prescribed with very low noise levels to mimic periodically-correlated surface wave dispersion measurements. We demonstrate how the incorporation of geodynamic and petrological constraints tightly recover these five unknowns, which will then imply the implicit retrieval of the complete patterns of upper mantle deformation, and correspondingly, the full elastic tensor.

3 Methodology

Since this work serves as a continuation to Magali et al. (2021b), this section only describes the appropriate changes made to the method to adapt geodynamic tomography to a subduction setting with known geometry.

3.1 Model parameterization

3.1.1 Thermal structure of a subducting slab

We begin by defining a 2.5-D temperature field T(**r**) that is constructed in a regular grid of size $N_x \times N_y \times N_z$ that extends symmetrically along the y-axis. The temperature field is expressed as the sum of a background temperature $T_{\text{background}}$ derived from a half-space cooling model, and a thermal anomaly δT which translates to:

$$T(\mathbf{r}) = T_{\text{background}}(\mathbf{r}) + \delta T(\mathbf{r}), \tag{1}$$

where $T_{\text{background}}$ is given by:

$$T_{\text{background}}(\mathbf{r}) = (1900\text{K} - 500\text{K})\,\text{erf}\left(\frac{z}{2\sqrt{\kappa t}}\right) + 500\text{K}, \tag{2}$$

where **r** is any arbitrary position in 3-D space defined by the coordinates **r** = [x,y,z], κ is the thermal diffusivity, z is depth, and t is the plate age in million years.

The anomaly δT is a subducting slab defined by three geometrical parameters: (1) dip angle θ, (2) length of the slab L, (3) thickness R, and one scalar parameter T_c that determines the magnitude of the temperature along the axis of symmetry of the slab. We model it in terms of a hyperbolic tangent function, tanh where it forces the temperature to be the coldest at the slab's symmetry axis, and that the spread of tanh relates to the thickness of the slab itself (*i.e.* the parameter R). The temperature anomaly is mathematically defined as:

$$\delta T(\mathbf{r}) = -\frac{T_c}{2}\left[1 - \tanh\left(\frac{\beta}{L_{\text{scale}}}\left(d - \frac{R}{2}\right)\right)\right] \tag{3}$$

where d is the distance from the slab's center axis to any point perpendicular to it, β controls the sharpness of the temperature gradient which is held at a fixed value, and L_{scale} is the length of the vertical domain which we set to 400 km. Fig. 1 shows the thermal structure of the subduction model viewed in 2-D (left panel) and in 3-D (right panel) using the aforementioned parameterization. The model parameters possess the following values: L = 150 km, θ = 35°, R = 120 km, T_c = 800 K.

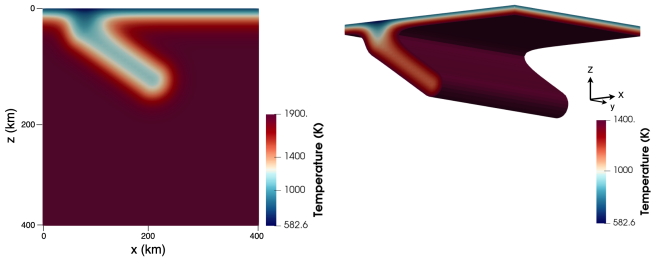

Figure 1 Thermal structure of a subduction zone parameterized in terms of geometrical points. The structure is rendered using the following input parameters: L = 150 km, θ = 35°, R = 120 km, T_c = 800 K. The left panel represents the vertical cross-section of the model whereas the right panel corresponds to the isovolumetric contour plot of the temperature field.

3.1.2 Medium rheology

The medium rheology is modeled following the Frank-Kamenetskii approximation to Arrhenius-type viscosity. This means that the influence of temperature onto viscosity is supervised by the activation coefficient E. The viscosity field η is given by:

$$\eta(\mathbf{r}) = \eta_0 \exp\left[-E\frac{T(\mathbf{r}) - T_0}{T_0}\right], \tag{4}$$

where η_0 and T_0 are reference values for viscosity and temperature, respectively. In the inversions, the total number of parameters to be inverted for are five: four of which L, θ, T_c, and R characterize the temperature field of the subduction model, and the latter E controls the sensitivity of the viscosity to temperature. We choose E as an unknown in order to demonstrate the ability of geodynamic tomography to constrain some properties of the medium rheology. This is essential because we expect that larger values of E make the cold slab more rigid, and thereby lessen the amount of strain-induced anisotropy across it. Since seismic data contain the surface manifestation of strain-induced anisotropy, they then provide potential clues about the rheological structure of the Earth's interior. The variables β, T_0, and

η_0 are held at fixed values throughout the inversion process. The model vector $\mathbf{m}$ is thus:

$$\mathbf{m} = [L, \theta, T_c, R, E]. \quad (5)$$

3.2 The forward problem

The complete forward problem proceeds as follows: (1) Given the temperature and viscosity fields described by Equations (1) and (4), respectively, we first numerically solve an instantaneous 3-D convection problem with temperature-dependent viscosity that is benchmarked against Samuel (2012, 2018). (2) Using the velocity field obtained from (1), we compute velocity gradients using finite differences. (3) Under a steady-state assumption, we then trace the flow backwards in time using fourth-order Runge-Kutta, and at each time step along the flow line, a local velocity gradient tensor is estimated. (4) We then track CPO evolution of olivine aggregates using `D-Rex` (Kaminski et al., 2004). This computes the anisotropic part of the elastic tensor. Later in the inverse approach, we replace step (2) with an artificial neural network (Bishop et al., 1995) whose architecture follows that of LeCun et al. (2015). The training data are comprised of a pair of flow lines with local velocity gradients at discrete time steps along the path (training input) and the deviatoric part of the elastic tensor predicted with `D-Rex` (training output). This speeds up the computation of anisotropy by several orders of magnitude (Magali et al., 2021b), and hence is befitting within a sampling-based inversion scheme (Hansen and Cordua, 2017; Köpke et al., 2018; Conway et al., 2019; Moghadas et al., 2020). (3) From the temperature field and the hydrostatic pressure, we derive the pressure and temperature dependence of the isotropic part of the elastic tensor using a thermodynamic model for a given bulk composition using `Perple_X` (Connolly, 2005, 2009; Stixrude and Lithgow-Bertelloni, 2011). The result from (2) and (3) is a complete elastic tensor at each point in space. (3) The last step involves computing synthetic surface wave dispersion curves using normal mode summation in a spherical earth (Smith and Dahlen, 1973) using `DISPER80` (Saito, 1988) and their azimuthal variations (Montagner and Nataf, 1986) from the elastic tensor. We refer the reader to Magali et al. (2021b), and Chapter 3 of Magali (2021) for a comprehensive description of the full forward problem.

3.3 Synthetic data

The synthetic data to be inverted consists of local surface wave dispersion measurements and their azimuthal variations at the surface. The form of the Rayleigh wave dispersion curve is the sum of an isotropic component $\mathbf{c}_{R,0}$ and its azimuthal variations $\mathbf{c}_1$ and $\mathbf{c}_2$:

$$\mathbf{c}_R(P, \psi) = \mathbf{c}_{R,0}(P) + \mathbf{c}_1(P)\cos(2\psi) + \mathbf{c}_2(P)\sin(2\psi), \quad (6)$$

and for Love waves we simply have:

$$\mathbf{c}_L(P) = \mathbf{c}_{L,0}(P), \quad (7)$$

where P is the period, and ψ is the azimuth of propagation. Notice that we have neglected the azimuthal terms for Love waves. Such simplifications are reasonable due to sparse azimuthal coverage and higher noise levels on Love waves relative to Rayleigh waves in real-Earth data (Maupin and Park, 2015).

3.4 Inversion method

Bayesian inversion is implemented where the solution is an ensemble of models (*i.e.* model parameters found in Equation (5)) distributed according to the posterior probability density function $p(\mathbf{m}|\mathbf{d_{obs}})$, accompanied by their uncertainty bounds. In this framework, Bayes' theorem is written as:

$$p(\mathbf{m}|\mathbf{d_{obs}}) \propto p(\mathbf{m})p(\mathbf{d_{obs}}|\mathbf{m}). \quad (8)$$

The parameter space is searched using a Markov chain Monte Carlo (McMC) algorithm. To produce reasonable acceptance rates, we employed an adaptive perturbation scheme.

3.4.1 Likelihood function

The likelihood function $p(\mathbf{m}|\mathbf{d_{obs}})$ quantifies how well the model parameters fit the observed data. Here we assume that the errors are uncorrelated and follow a univariate Gaussian distribution with zero mean, and variance σ_c^2, the likelihood function corresponding to a single dispersion measurement can be written as:

$$p(\mathbf{c_{obs}}|\mathbf{m}) = \frac{1}{(2\pi\sigma_c^2)^{N/2}} \exp\left[\frac{-||\mathbf{c_{obs}} - \mathbf{c_{est}}||^2}{2\sigma_c^2}\right], \quad (9)$$

where $\mathbf{m}$ is the model vector, N is the number of discrete periods, σ_c^2 is the estimated variance of the data noise, $\mathbf{c_{obs}}$ is the observed synthetic data to be inverted, and $\mathbf{c_{est}}$ is the synthetic data estimated during the inversion process. The likelihood functions of the 2θ terms can be cast in the same manner.

3.4.2 Prior distribution

We assume the model parameters to be independent. In this way, the prior distributions for each model parameter are separable and can be expressed as a product of each distribution:

$$p(\mathbf{m}) = \prod p(L)p(\theta)p(R)p(T_c)p(E). \quad (10)$$

Each prior on the model parameters follows a uniform distribution with wide bounds to avoid imposing hard constraints from the prior. Such a setup mimics a scenario where prior knowledge about the regional setting is scant and thus the solution to our inverse problem is more likely driven by the information provided by the data. The prior bounds are as follows: (1) 100 km - 200 km for L, (2) 80 km - 150 km for R, (3) $20° - 45°$ for θ, (4) 500 K to 1000 K for T_c, and (5) 5 to 12 for E.

3.4.3 Generation of new models along the Markov chain

We use a a Markov chain Monte Carlo (McMC) algorithm to search the parameter space that could explain the data. The sampler initiates by randomly drawing a set

of L, R, θ, T_c, and E values within the prior bounds followed by the evaluation of the likelihood function. Then at each iteration in the Markov chain, a new model $\mathbf{m}'$ is proposed by randomly selecting one of the possible set of moves:

1. Vary the length of the slab L. The slab length is perturbed according to a univariate Gaussian distribution centered at the current value of L.

2. Vary the dip angle θ. The dip angle is perturbed according to a univariate Gaussian distribution centered at the current value of θ.

3. Vary the thickness of the slab R. The slab thickness is perturbed according to a univariate Gaussian distribution centered at the current value of R.

4. Vary the temperature of the slab T_c. The slab temperature is perturbed according to a univariate Gaussian distribution centered at the current value of T_c

After choosing one of the four possibilities, the proposal is always accompanied by the perturbation of E. The activation energy is perturbed using a univariate Gaussian distribution centered at the current value of E.

4 Full forward procedure to predict surface wave measurements from the subduction model

Tab. 1 summarizes the true model parameters used to describe the thermal and rheological structure of the synthetic subduction zone. Note that the other scalar variables uninvolved in the inversion procedure, such as the dimensionless parameters defining the Rayleigh number, are preserved as in Magali et al. (2021b). When computing CPO anisotropy with D-Rex, we use the active slip systems of olivine corresponding to dry upper mantle conditions, and estimate the evolution of the texture onto ∼2000 olivine crystals for 10 My. Other parameters such as the grain boundary mobility and the threshold volume fraction for grain boundary sliding are taken from the reference D-Rex model (Kaminski et al., 2004).

Model parameter	Assigned value
L	150 km
R	120 km
θ	35°
T_c	800 K
E	11.0

Table 1 True model parameters defining the thermal structure of the subduction model.

The instantaneous flow is computed in a 400 km × 400 km × 400 km box with a 6.25 km × 6.25 km resolution. Tangential velocities are prescribed at the top to replicate real Earth subduction dynamics. The bottom and lateral boundary conditions are free-slip.

Fig. 2a shows the vertical cross-section of the 3-D instantaneous flow field induced by subduction. We observe one of the conspicuous features of subduction-induced flow, that is the existence of a local convection cell beneath the slab tip attributed to retrogade slab motion. This is accommodated by the existence of back-arc motion towards the trench made responsible mainly by trench suction and in part by the induced leftward motion due to the imposed plate velocity across the overriding plate. This also ensures flow ascension in front of the slab. The vigorous mixing observed across the sub-slab mantle resembling roll-back motion is mainly influenced by horizontal boundary effects. Such effects can be reduced by increasing the size of the model domain. Nevertheless, most features observed across the vertical cross-section are mainly predisposed by poloidal flow (*i.e.*, buoyancy-related motion). In essence as with any divergence-free vector field, our velocity field can be decomposed into a poloidal component, and a toroidal component which relates to horizontal flow due to the presence of lateral viscosity contrasts (Gable et al., 1991; Bercovici, 1995). Since we imposed temperature-dependent viscosity, we are compelled to deal with toroidal motion due to lateral variations in viscosity as shown in Fig. 2b (*i.e.* the horizontal projection of the flow whose plane is normal to the $z-$axis) where we observe some local vorticities around the slab edges.

Fig. 3 shows the vertical cross-section of the finite strain representation of the subduction model. Solid black lines pertaining to the orientation of the long axis of the finite strain ellipsoid (fse) are superimposed on top of the natural strains (*i.e.*, amplitude of finite deformation in terms of the natural logarithm of the ratio between the long and short axes of the fse). Finite strain orientations to first-order tend to be parallel to the direction of flow, however, may lag behind in some instances where deformation rapidly varies along the flow trajectory (Kaminski and Ribe, 2002). The absence of deformation correlates well with the presence of the fortified and highly-viscous slab.

From the velocity field, we gain access to the macroscopic velocity gradients by finite differencing. The 3-D map of the local velocity gradient in conjunction with the temperature field are utilized to construct an elastic model of the synthetic subduction zone using a micromechanical model for CPO evolution for the anisotropic part, and a thermodynamic model for the isotropic part, respectively. At any arbitrary location in 3-D space, the elastic model contains the full elastic tensor. Since it is arduous to interpret a fourth-rank tensor, it is often convenient to decompose $\mathbf{S}$ into a specific symmetry class to better analyse its properties. Fig. 4 illustrates the vertical cross-section of the elastic constants A_0 related to $PV-$waves and L_0 related to $SV-$waves associated with the subduction model. The elastic constants are computed from the elastic projection of $\mathbf{S}$ to an azimuthally-averaged VTI medium (Montagner and Nataf, 1986). Both panels robustly map the cold subducting slab with L_0 exhibiting sensitivity to temperature variations more fervently than A_0. Since the con-

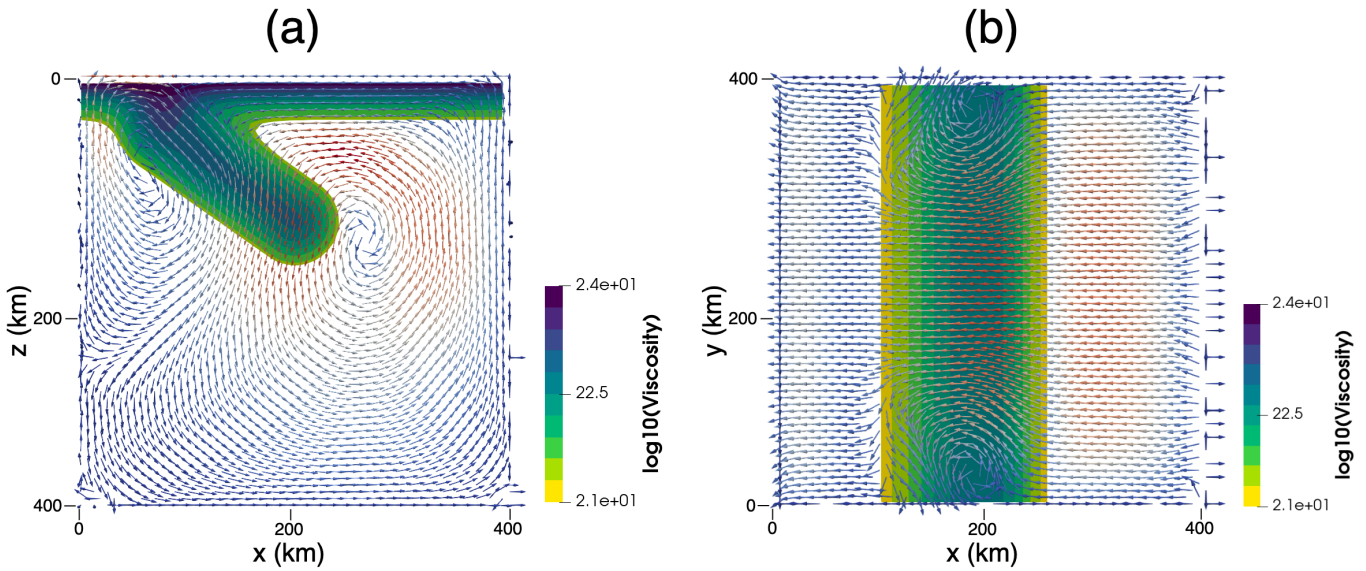

Figure 2 Instantaneous velocity field induced by subduction. The effective viscosity in log units is superimposed. Model domain is of the size 64 × 64 × 64 elements, free-slip boundary conditions are imposed at the lateral and bottom sides. Opposing plate velocities are prescribed at the top to drive horizontal motion. (a) Vertical cross-section of the velocity field. (b) Overhead view of the velocity field at a depth of ∼ 100 km. Figure (b) illustrates the significance of lateral viscosity variations to produce toroidal fluid flow.

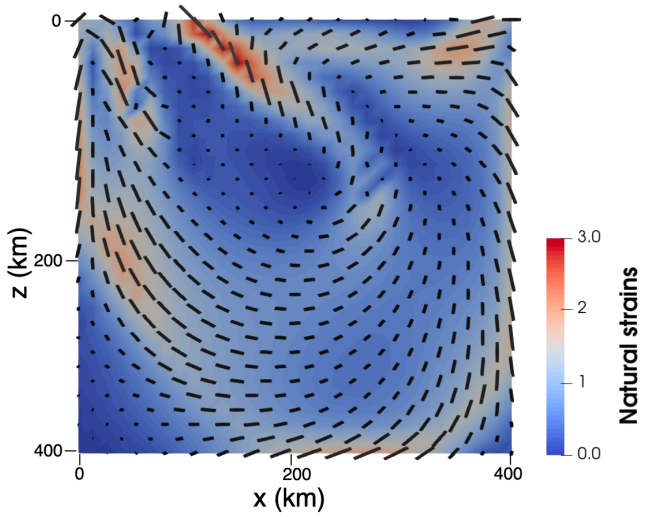

Figure 3 Cross-sectional view in the $\mathrm{xz}-$ plane of the natural strains (*i.e.*, amplitude of the fse in terms of the natural logarithm of the ratio between the long and short axes). Solid black lines are attributed to the orientation of the long axis of the fse. Finite strain framework is usually used as a proxy to infer convective flow in the mantle.

stants A_0 and L_0 are not the isotropic averages of the fast and slow velocities but a linear combination of the elastic tensor, they possess small anisotropic perturbations thus explaining the presence of smearing in some areas of the maps.

On the other hand, Fig. 5 represents the vertical cross-section of $S-$wave radial anisotropy ξ (left panel) and of the amplitude of total anisotropy in terms of the anisotropy index (*i.e.*, norm fraction of the elastic tensor with respect to the isotropic component) (right panel). As observed, regions of positive radial anisotropy $\xi > 1$ correlate well with horizontal flow and of negative radial anisotropy $\xi < 1$ with vertical flow. In terms of the anisotropy index, the entrained mantle wedge adjacent to the plunging slab, and beneath the back-arc produced the most CPO due to shear deformation initiated by slab pull and reinforced by trench suction. Strong anisotropy produced across the shallower depths of the sub-slab can be attributed to roll-back motion augmented by boundary effects. Across the slab itself, we expect $\xi \approx 1$ since the material is designed to mimic rigid plates that withstand deformation. This is also observed at the right panel where the anisotropy index across the slab appears to be close to zero. Thus in this case, the subducting slab can be regarded as isotropic since no CPO is generated due to its resilient rheological integrity. The presence of small-scale artifacts in the anisotropic structures may be attributed to numerical errors associated with the forward calculations.

From an elastic medium built from the spatial distribution of $\mathbf{S}$, it is now possible to compute 2-D phase velocity maps and their azimuthal variations. For instance, Fig. 6 shows a map of the computed phase velocity and azimuthal anisotropy for Rayleigh waves at 100 s. The increase in velocity on the left portion of the map shown in Fig. 6a indicates the influence of the cold subducting slab. In Fig. 6b, the characteristic blue margin in between the yellow regions corresponds to the slab itself. This is also delineated by the shortening of the fast axis of azimuthal anisotropy within its vicinity (solid black lines). Although the orientation of the fast axis is a sufficient proxy to infer the horizontal projection of flow, it may still fail to render some important characteristics such as the presence of a toroidal component in the flow. This is because azimuthal anisotropy in surface waves is an integrated effect of the elastic anisotropy with depth. Furthermore, the latter depends on the deformation trajectory. Hence, absolute flow

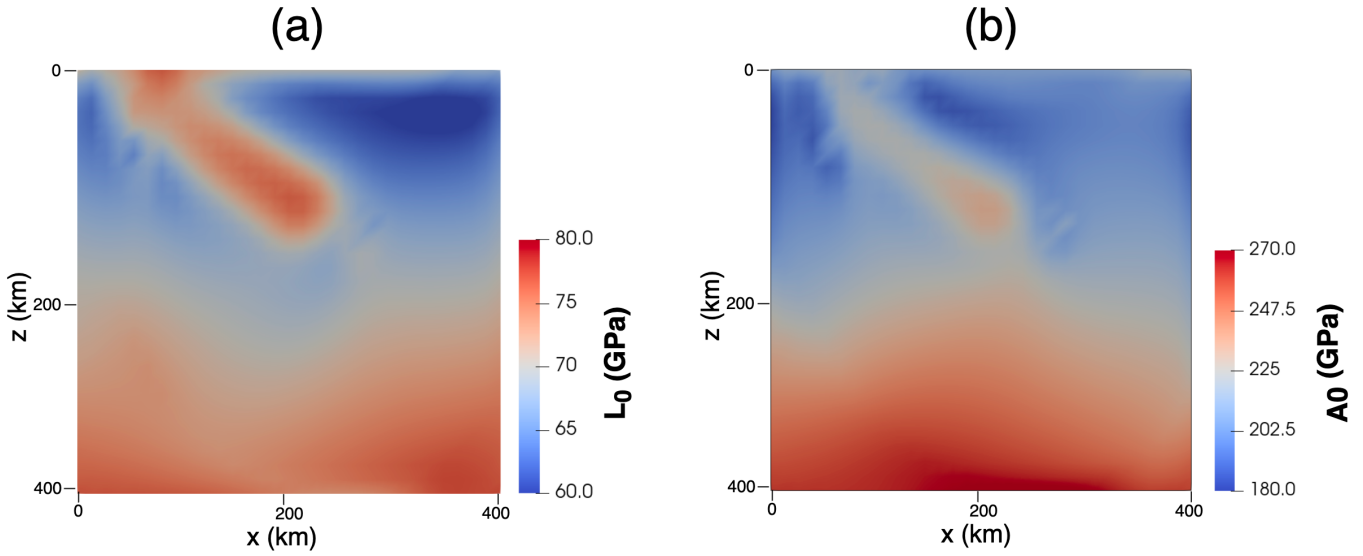

Figure 4 Cross-sectional view in the $\mathrm{xz}-$ plane of the elastic constants L_0 (left panel) and A_0 (right panel). Since elasticity strongly depends on temperature, we can easily map the cold subducting slab in the seismic models. The cross sections are taken at the center of the $\mathrm{y}-$ axis.

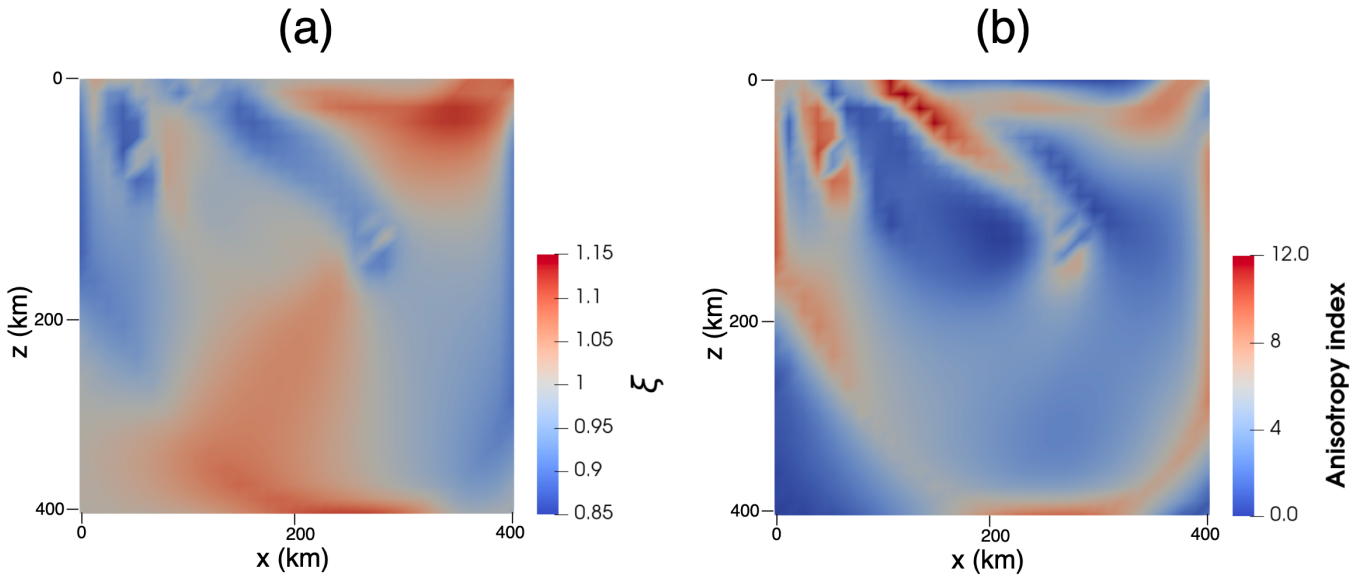

Figure 5 Cross-sectional view in the $\mathrm{xz}-$ plane of the $S-$wave radial anisotropy ξ (left panel) and the anisotropy index expressed in terms of the tensor norm fraction of $\mathbf{S}$ with respect to its isotropic component (right panel). The cross sections are taken at the center of the $\mathrm{y}-$ axis.

velocities may be well away from the orientation of its fast propagation. Finally, the deformation induced by subduction seemingly produces about 2% azimuthal anisotropy in surface waves which spreads out almost evenly throughout the map and is only restricted by the existence of the slab.

5 Inversion results

Using the values of the model parameters summarized in Tab. 1, we generate synthetic surface wave dispersion curves and their azimuthal variations at periods between 10 and 200 s with 10 s intervals. The complete data consist of a regular array of 8×8 locations containing $\mathbf{c}_R$, $\mathbf{c}_L$, $\mathbf{c}_1$, and $\mathbf{c}_2$ spanning the entire surface. The synthetic data are computed based on the full elastic tensors (*i.e.* with 21 independent coefficients) calculated with `D-Rex`.

We add Gaussian uncorrelated noise onto $\mathbf{c}_{R,0}$, $\mathbf{c}_{L,0}$, $\mathbf{c}_1$, and $\mathbf{c}_2$. We assign very low noise levels for $\mathbf{c}_{R,0}$ and $\mathbf{c}_{L,0}$ with $\sigma_{R,L}$ = 0.001 km s^{-}1 to mimic periodically-correlated surface wave dispersion measurements. Conversely, the azimuthal variations are assigned with $\sigma_{1,2}$ = 0.005 km s^{-}1. Fig. 7 shows a synthetic surface wave dispersion curve with and without added noise at one specific geographical location.

The inversion consists of 20 independent Markov chains containing 40 000 samples each initiated at a random model (*i.e.,* values for L, θ, R, T_c, and E are randomized for all chains) to ensure loose compliance to the initial model. Job array processing has been imple-

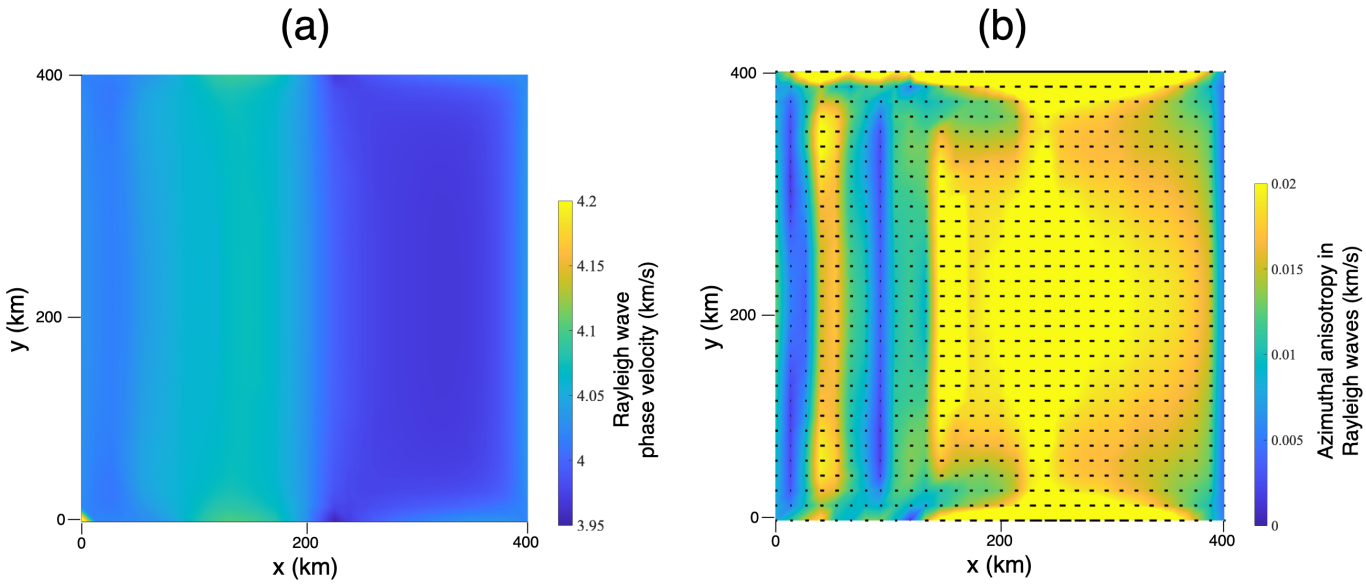

Figure 6 Phase velocity maps derived from a 3-D deforming upper mantle beneath a subduction zone at 100s period. (a) Rayleigh wave phase velocity (km/s). (b) Azimuthal anisotropy in Rayleigh waves (km/s). The solid black lines correspond to the direction of the fast propagation axis. Surface wave maps always lie along the $\mathrm{xy}-$ lateral plane.

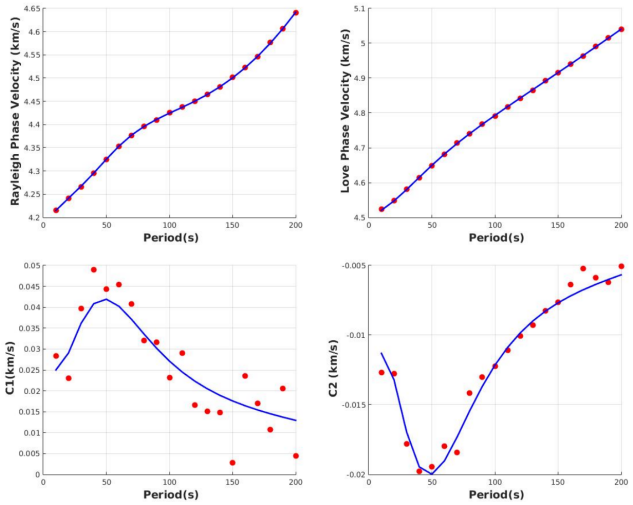

Figure 7 Synthetic surface wave dispersion curves from 10 to 200 s at a given geographical location (blue lines). The data used in the inversions have been added with Gaussian uncorrelated noise (red circles).

mented where each Markov chain is assigned with one element of the job array. Each job array then contains one task per node. Meanwhile for each task (and hence each node), 12 CPUs are assigned for multi-threading flow computations with OpenMP (OpenMP Architecture Review Board, 2008). As for the rest of the computations involved in the full forward procedure, we use a serial implementation for each task. On average it takes approximately 10 seconds to complete one McMC cycle (*i.e.* model proposition + forward computation + likelihood function computation).

We demonstrate two cases: (1) an isotropic inversion and an (2) anisotropic inversion (*i.e.*, geodynamic tomography). Both cases are imposed with wide uniform priors allowing for more mobility when searching the parameter space. For efficient sampling, we commence geodynamic tomography by first employing an isotropic inversion. Once the independent chains have converged in this phase, we then proceed with the actual anisotropic inversion procedure. It is important to emphasize that we implement an artificial neural network (ANN) algorithm to approximate `D-Rex`. Since the current architecture of the network is problem-specific, it is designed based on training data generated by flow models produced by a family of thermal subduction models described by Equations (1), (2), and (3).

5.1 Marginal posterior probability distributions of the recovered model parameters

Figs 8 and 9 show the 1-D marginal posterior probability distribution on each model parameter (diagonal panels) and the joint marginal posterior probability distribution between a pair of model parameters (off-diagonal panels) to explore possible trade-offs for isotropic inversion and anisotropic inversion, respectively. The red lines and the black circles indicate their correct values. Both cases have exhibited a single misfit minima for the model parameters that define the thermal structure of the subduction model. However by incorporating geodynamic and petrological constraints, we observe that the entirety (this includes E) are much more tightly constrained than the isotropic case, as evidenced by the considerable decrease in the spread of the distributions. The narrow widths of the posterior distributions are also a manifestation of the low noise levels accounted for in the inversions. Between these two effects, it can be implied that the imposition of geodynamic constraints contributes far more toward the robustness of the solutions than the usage of low-noise data. Finally, the existence of a linear trade-off between

a pair of parameters appears to be widespread. Such behavior is most apparent between the temperature of the slab T_c and the slab geometry, particularly L and R. This is likely due to the accommodation of the increase in the slab temperature by an increase in its size.

It is expected that isotropic inversion hardly constrains E since isotropic velocities do not depend on deformation history but are directly derived from temperature and pressure for a given chemical and mineralogical composition. Contrastingly, anisotropic inversion effectively constrains E although the result is clearly biased as it is observed to differ from its true value. In actuality, bias exists in all the parameters at least except for the length of the slab L. Thus the existence of misfit minima that are not in agreement with the true model parameters can either be explained by the use of an incorrect surrogate model in the inversion or the incapability of surface wave data to recover the synthetic subduction zone.

To demonstrate that surface waves can recover simple models of subduction, we include another test where the observed surface wave data is generated by an elastic medium predicted with ANN (*i.e.* the surrogate model). Fig 10 now shows the 1-D and joint marginal probability distributions as a result of this new numerical experiment. Here, we notice the mitigation of model uncertainties through the narrowing of the distributions. Furthermore, we also observe how these distributions are centered at the true values of the model parameters. Based on these results, it is now clear that the behavior exhibited in Fig 9 is a direct consequence of using D-Rex in the full forward procedure and using a surrogate model based on ANN in the inversion. Indeed, implementing the correct forward model to compute anisotropy decreases model uncertainties and eliminates the bias. Since these forward models tend to be computationally expensive when employed with direct-search algorithms, it is imperative to utilize fast-forward approximations such as neural networks. This however necessitates the inclusion of additional training data and/or possibly the partial or complete overhauling of the network architecture.

5.2 Retrieval of the temperature field and some implicitly computed seismic anisotropy variables

Fig. 11 illustrates the reconstructed mean temperature field coming from the 20 Markov chains from both inversions (top panels) and their corresponding uncertainties in terms of the standard deviation (bottom panels). By visual inspection, we notice that the mean temperature field from the isotropic inversion (Fig. 11a) is not much different from the anisotropic case (Fig. 11b). Due to the low levels of noise in the data, anisotropy does not bring much in the recovery of the temperature field. However in the case of larger noise levels, the inclusion of anisotropy in the inversions would be more beneficial. The standard deviation conveys a different story however, as observed by its smaller amplitude in the case of geodynamic tomography (Fig. 11d). In both cases, the uncertainties are seemingly clustered across subducting slab with two discernible plunging stripes. This indicates a state of relaxation, or more preferably, convergence of the Markov chains towards a stable solution. The plunging stripes therefore are a result of a random-walk behavior of the subducting slab about its center. The center of the slab is delineated by the area of low uncertainty partitioning the two plunging stripes of high uncertainties.

Fig. 12 shows the 1-D depth marginal posterior probability profiles at a given location for temperature, $S-$wave radial anisotropy ξ, peak-to-peak azimuthal anisotropy in terms of $2G/L_0$ where G is the horizontal azimuthal dependence of L_0, and the azimuth of the fast direction of azimuthal anisotropy inferred from geodynamic tomography. We successfully jointly recovered azimuthal and radial anisotropy without having to explicitly invert for the elastic tensor. One of the key advantages of geodynamic tomography is its capacity to capture intricate and highly complex features, as exemplified by the recovered amplitude of azimuthal anisotropy and its fast azimuth. Furthermore, one of the long standing problems of conventional surface wave tomography is the depletion of its resolving power with depth since its energy is mostly concentrated across the surface. Here we have demonstrated the ability of geodynamic tomography in the apparent eradication of this effect as evidenced by the preservation of the width of the posteriors in depth.

Lastly, geodynamic tomography offers the capability to resolve 3-D structures of any implicitly computed variable. As a demonstration, Fig. 13a illustrates the S-wave radial anisotropy ξ and Fig. 13b, the anisotropy index obtained from the mean temperature model. A recurring issue is the underestimation of seismic anisotropy in comparison with the true model (Fig. 5) due to the use of an approximate forward operator to model CPO evolution. This is compensated by the weakening of the slab rheology through the reduction of the activation coefficient (Fig. 9 bottom right panel), in order to produce larger levels of anisotropy.

6 Discussion

Most of the limitations of the method have already been laid out in (Magali et al., 2021b). There we discussed several areas for improvement which include but are not limited to: (1) the inclusion of other types of data such as gravity anomalies for better model constraints, (2) the usage of a generalized surrogate model for computing anisotropy, and (3) the underlying assumptions in mantle composition. Here, we discuss the limitations and the resulting implications of using thermally-driven instantaneous models of subduction. Finally, we discuss what the future holds for the method, that is, its potential application to a real Earth problem.

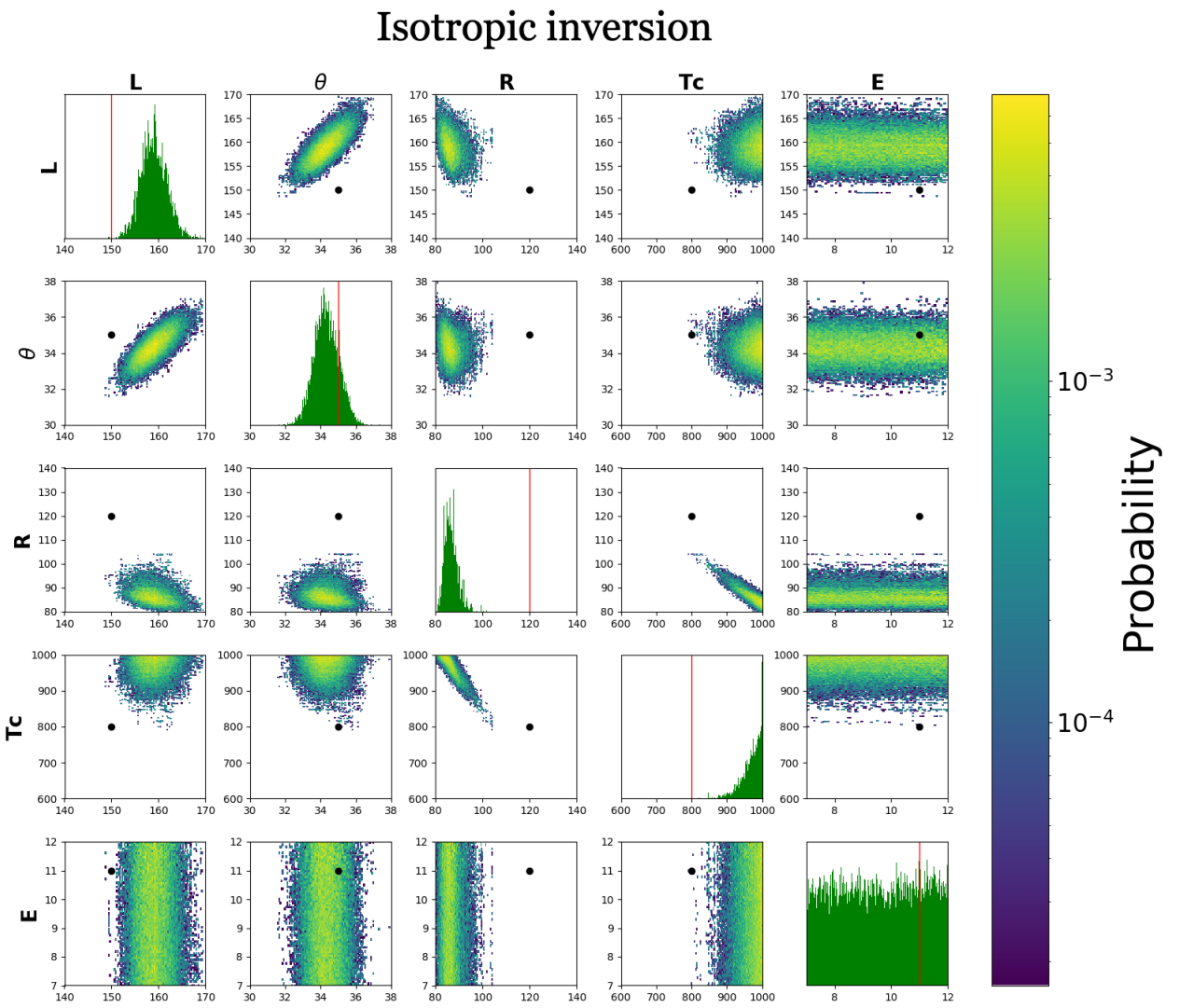

Figure 8 Posterior probability distribution in the five-dimensional parameter space inferred from the isotropic inversion $p(\mathbf{m}|\mathbf{c}_R, \mathbf{c}_L)$. Diagonal panels show 1-D marginal distributions for each model parameter. Off-diagonal panels show 2-D marginal distributions and depict possible trade-offs between pairs of model parameters. The red vertical lines and the black markers indicate the true model values for the diagonal and the off-diagonal panels, respectively. The intensity pertains to the level of posterior probability (*i.e.*, high intensity means high probability, and thus low misfit).

6.1 Comments on the use of instantaneous subduction model

Our numerical experiments assume that the subduction geometry is already known to a certain degree given the ever-growing geophysical data available. This is similar to the geodynamic inversions demonstrated by Baumann and Kaus (2015). Because of this, the prior bounds we have selected for the model parameters such as the slab length being 100 km $-$ 200 km or the angle of subduction being $20° - 45°$ are reasonable. However, we acknowledge the existence of some end-member slab geometries such as those whose dip angle is nearly vertical (*e.g.* Kermadec and Marianas) and those whose dip angle is constant but whose slab length is $>$ 200 km and some even penetrating the transition zone (*e.g.* Central and South Kurile) as evidenced by (Fukao et al., 2009). It is expected that increasing the range of the prior would not have a substantial effect on the shape of the posterior due to the relatively small noise levels prescribed in the observed data (*i.e.,* the narrow shape of the likelihood compared to the prior). Nevertheless, we can ascribe the subduction geometries coming from our prior distribution to short and young, or even detached slabs.

It has already been shown that upper mantle minerals deform by dislocation creep to facilitate the development of CPO (Karato and Wu, 1993; Hirth and Kohlstedf, 2003). Thus, it would make sense to implement stress-dependent rheologies (*i.e.* non-Newtonian flows) in our geodynamic models. Geodynamic tomography is still at the 'proof-of-concept' stage, and so incorpo-

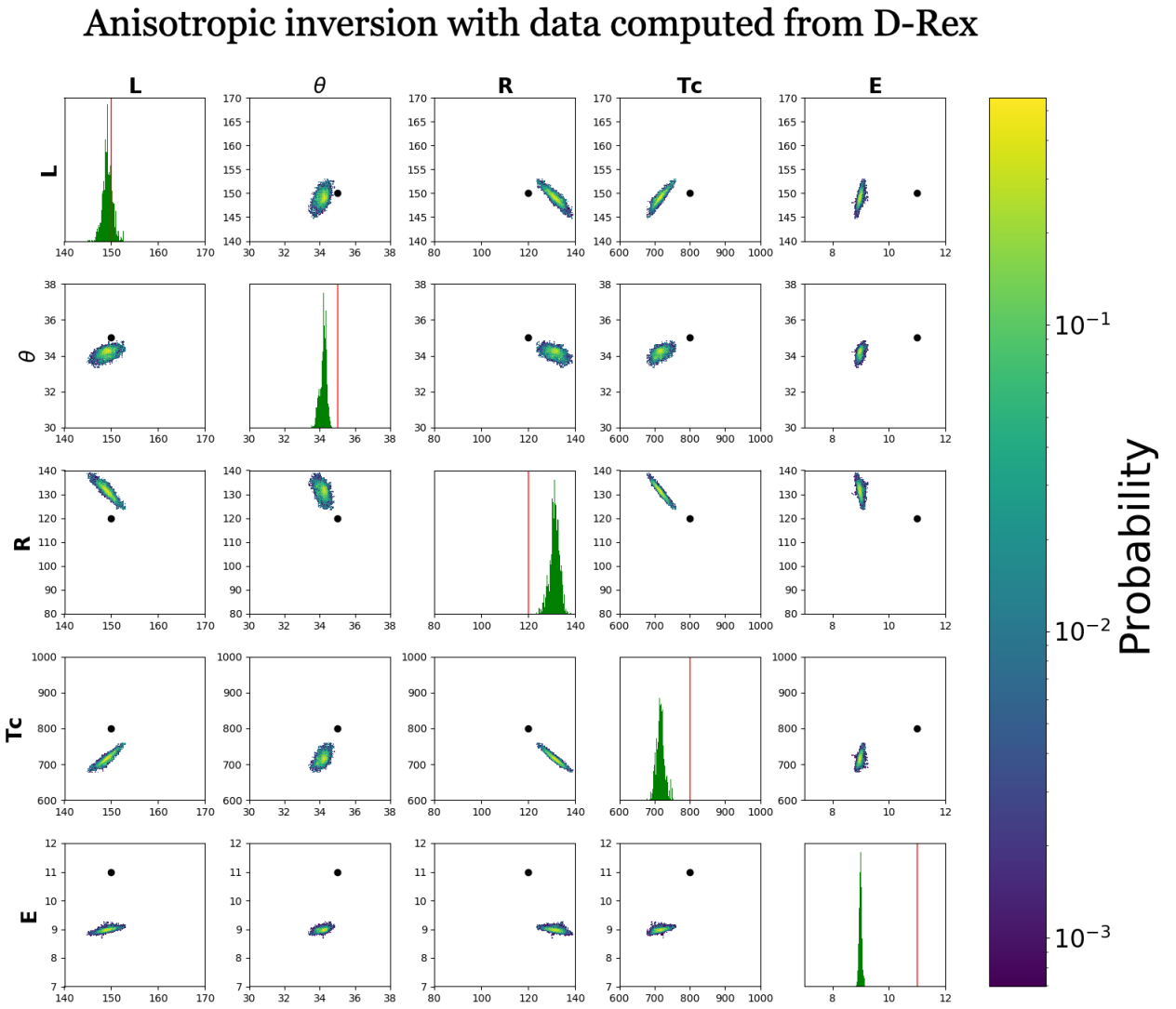

Figure 9 Posterior probability distribution in the five-dimensional parameter space inferred from the anisotropic inversion $p(\mathbf{m}|\mathbf{c}_R, \mathbf{c}_L, \mathbf{c}_1, \mathbf{c}_2)$. With D-Rex used to generate the observed data, the marginal distributions are not centered at the true values. The narrowness of the distributions is an imprint of the low noise levels prescribed in the observed data.

rating stress-dependent rheologies onto our instantaneous flow model would require additional effort for optimization (*i.e.* speeding-up flow computations while minimising sharp lateral viscosity contrasts) especially when considering a sampling-based inversion scheme where the flow has to be calculated numerous times. However, it has been reported that Newtonian flows could replicate some aspects of non-Newtonian flows by varying the activation energy (Christensen, 1983; Billen and Hirth, 2005). Still, a Newtonian rheology remains valid when considering the large scale features of subduction-induced mantle flow (Becker et al., 2003; Piromallo et al., 2006), and especially when we expect small-scales to be tomographic-filtered by long-period seismic data (Magali et al., 2021a).

Finally, a steady-state assumption when back-tracing flow streamlines may not be applicable in regions where transient flow is predominant. As pointed out by Faccenda and Capitanio (2012, 2013), steady-state assumptions imposed onto convergent margins produce anisotropic patterns in that region that are largely biased. A more consistent way of computing anisotropy is to track the evolution with time of the path traversed by several tracer particles, incorporate texture evolution models at each time step, and compute how much strain is accrued by the process as they get forward advected (Faccenda, 2014; Chang et al., 2016). Indeed this can be one of the futures avenues to be delved upon to improve geodynamic tomography. With the steady-state assumption, we anticipate that the anisotropy recovered away from the slab edges, and across the sub-slab mantle or the mantle wedge to remain robust (MacDougall et al., 2017), and close to the convergent margin and slab edges to be interpreted with caution.

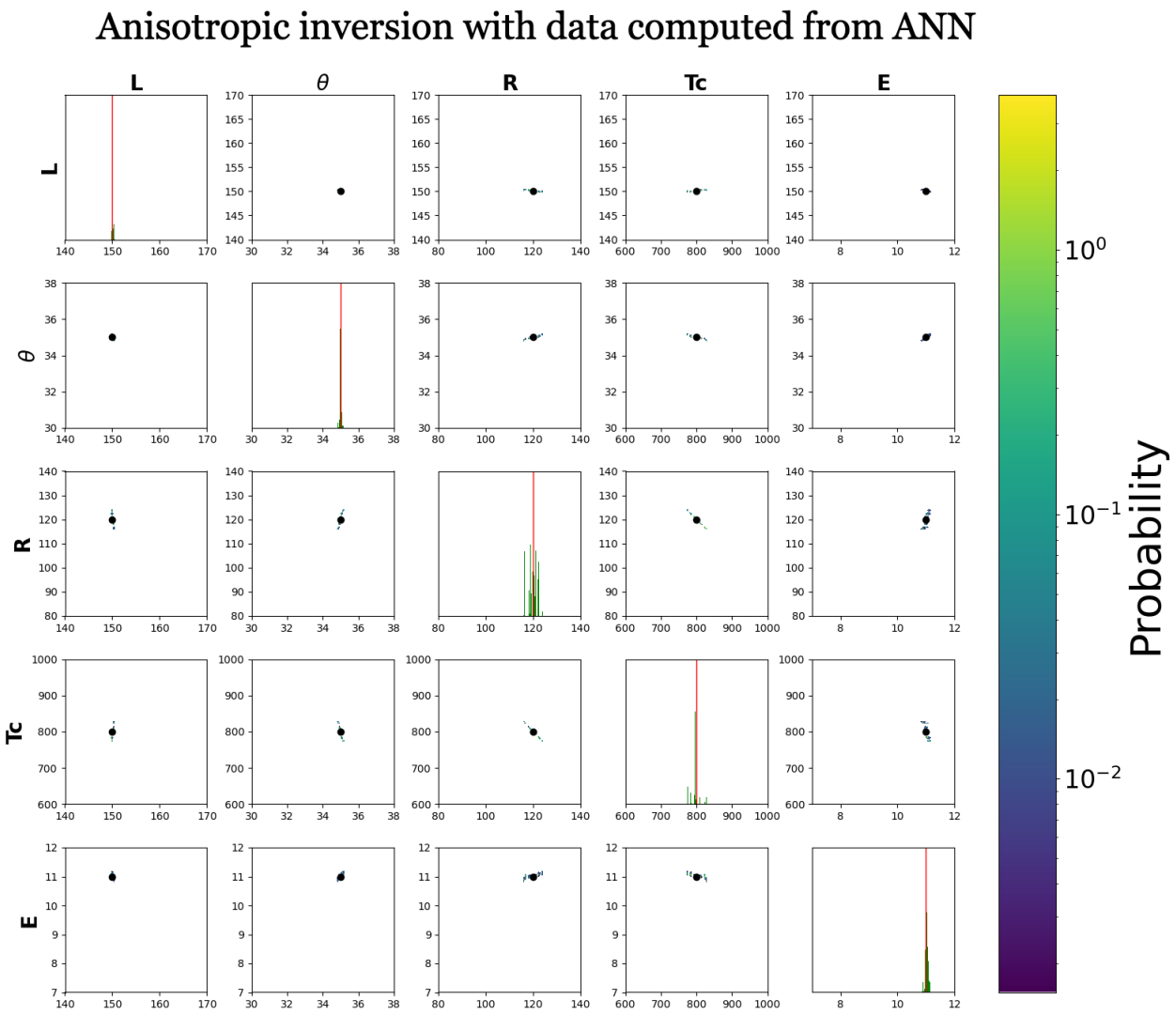

Figure 10 Posterior probability distribution in the five-dimensional parameter space inferred from the anisotropic inversion $p(\mathbf{m}|\mathbf{c}_R, \mathbf{c}_L, \mathbf{c}_1, \mathbf{c}_2)$. Here, the observed surface wave data is generated coming from an elastic medium predicted with neural networks. By using the correct surrogate model to match the one implemented in the inverse procedure, we observe how the marginal distributions are centered on their respective true values. This numerical experiment confirms that the bias and the model uncertainties observed in Fig. 9 results from the use of an ANN-based surrogate model to compute anisotropy.

6.2 Potential application to real surface wave dispersion measurements

Now that we have shown the capability of geodynamic tomography to recover synthetic structures close to real geodynamic settings, it is obvious that the next step is to apply the method to real Earth data. As such, this section briefly explains some forthcoming strategies to fully implement the method.

To recover the present-day thermal structure of the upper mantle from the inversion of real surface wave data, the inversion strategy should consist of three major stages: (1) In the first stage, we assume that surface wave dispersion maps within the desired period range are readily available. This is arguably the case in most places where surface wave dispersion measurements are widely available thanks to an ever growing amount of seismic records. From these maps spanning the entire geographical surface, we then invert local isotropic Rayleigh wave phase velocity dispersion curves for 1-D depth isotropic V_S models. (2) From the 1-D structures, the second stage involves the estimation of 1-D depth profiles of temperature T using first-order scaling relations between V_S and T. A more elaborate yet more computationally demanding approach is the inverse implementation of self-consistent thermodynamic modeling to infer T from V_S for any given bulk composition. The 1-D depth profiles of temperature can then be juxtaposed followed by smoothing through various interpolation schemes to build a smooth 3-D temperature field.

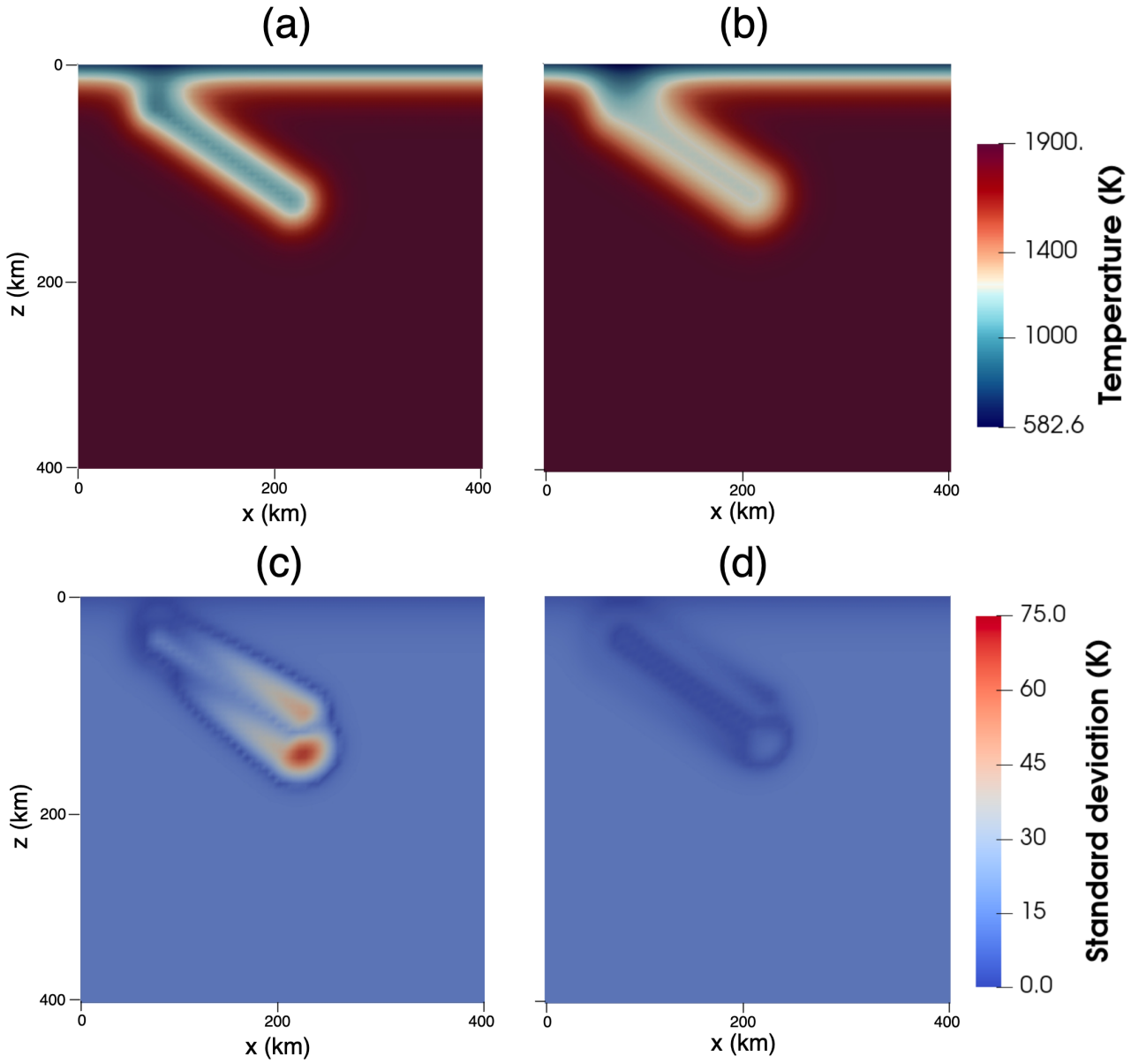

Figure 11 Upper panel: Cross-sectional view in the $\mathrm{xz}-$ plane of the mean temperature field recovered from (a) isotropic inversion, and (b) anisotropic inversion. Lower panel: Standard deviations around the mean temperature fields from (c) isotropic inversion, and (d) anisotropic inversion. These cross-sections are taken at the center of the $\mathrm{y}-$ axis.

(3) The last stage is geodynamic tomography itself, that is, using the 3-D temperature field inferred from the previous stage as the initial model to iteratively update its structure by inverting anisotropic surface wave dispersion curves. Fig. 14 is a schematic representation of this three-step inversion strategy.

7 Conclusion

We have tested the applicability of geodynamic tomography to a 3-D deforming upper mantle induced by subduction. Isotropic Love and Rayleigh wave phase velocity measurements and their azimuthal variations at a given location were jointly inverted to recover the 3-D thermal structure of a synthetic subduction zone. The method is cast in a Bayesian inversion procedure where the solution is an ensemble of unknown model parameters defining the thermal and rheological structure of the subduction zone, distributed according to a posterior probability density function.

In the process, not only do we successfully recover the desired thermal structure, we have also constrained the complete pattern of upper mantle deformation induced by subduction, and provided a quantitative interpretation on how these deformation patterns translate to seismic anisotropy that could potentially be imaged by seismic tomography. We have shown that the Bayesian framework propounds the capability to render marginal posterior probability distributions not only of the unknown parameters, but also of any implicitly computed variable such as deformation and anisotropy through geodynamic and texture evolution modeling, and quantify their associated uncertainty limits.

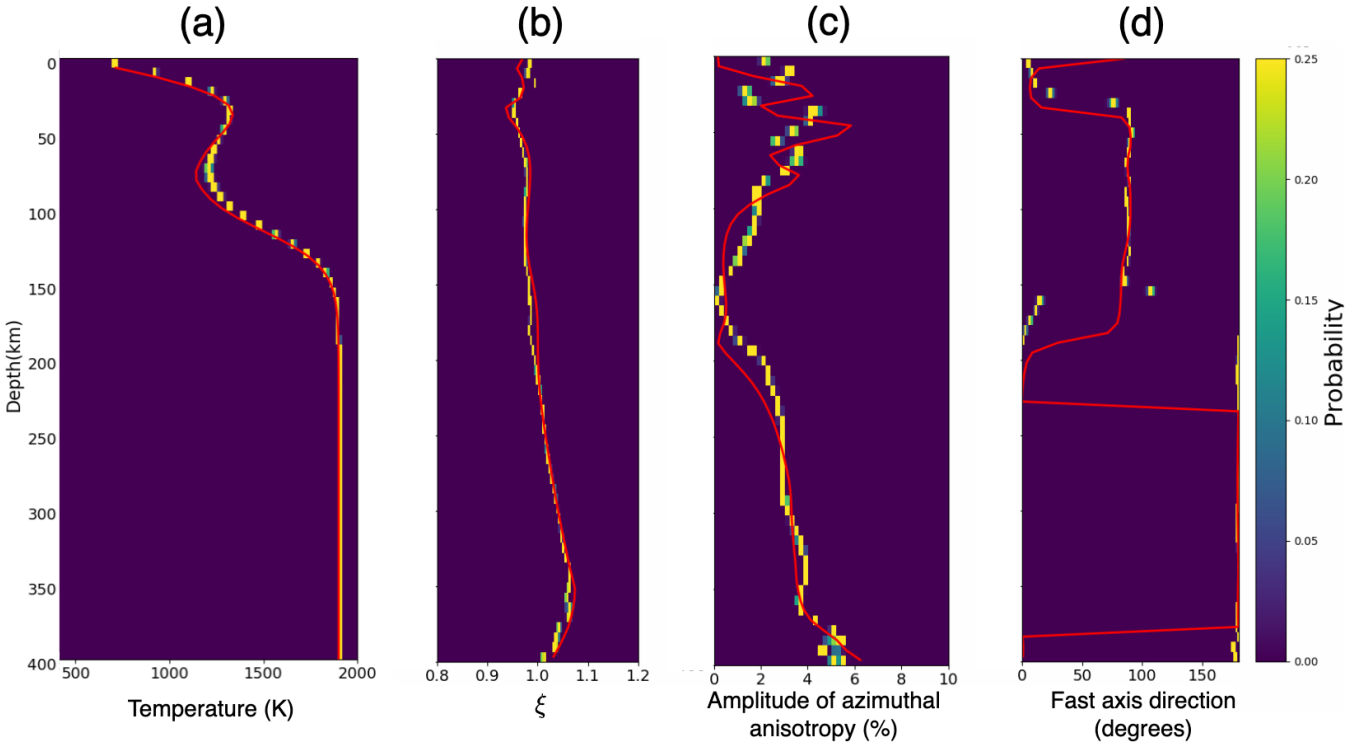

Figure 12 1-D marginal posterior probability profiles with depth of several variables inferred from geodynamic tomography. (a) Temperature. (b) $S-$wave radial anisotropy ξ. (c) Amplitude of azimuthal anisotropy in terms of $2G/L_0$ where G is an elastic constant corresponding to the horizontal azimuthal dependence of L_0. (d) Azimuth of the fast direction of azimuthal anisotropy. The depth profiles of temperature and ξ are taken at ($x = 125$ km, $y = 225$ km). To show that azimuthal anisotropy is also well-constrained, we took the depth profile at ($x = 175$ km, $y = 225$ km), where the patterns of azimuthal anisotropy are highly complex. Geodynamic tomography offers the capability to constrain seismic anisotropy. The solid red lines indicate the true structures.

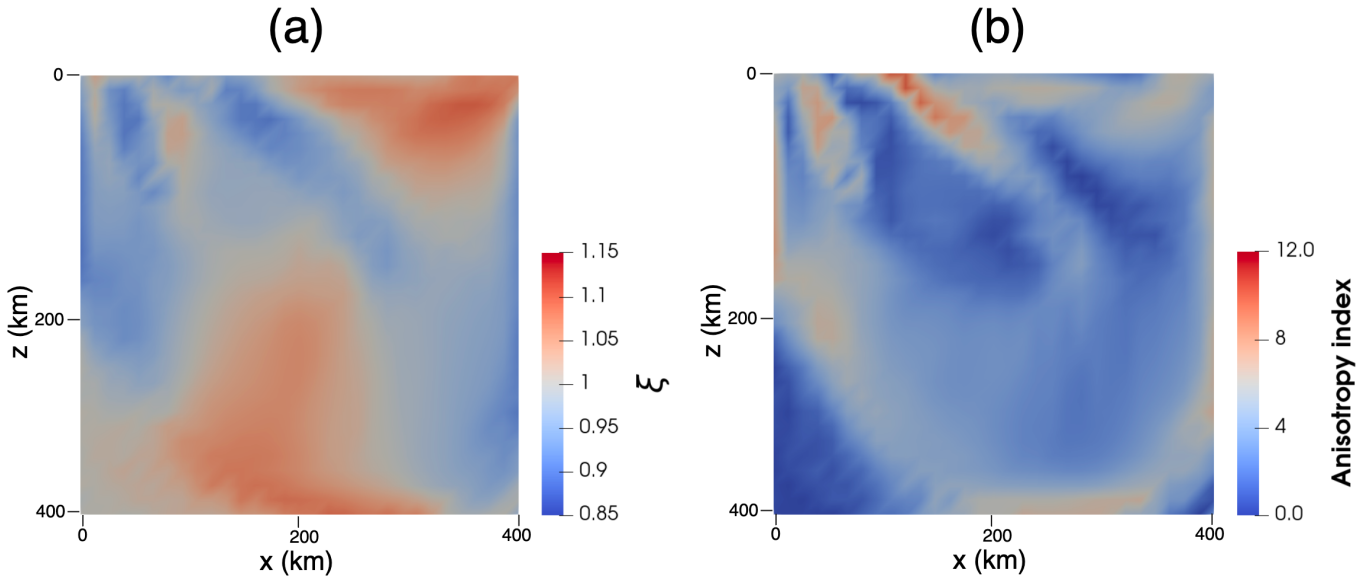

Figure 13 Cross-sectional view in the $\mathrm{xz}-$ plane of the $S-$wave radial anisotropy ξ (a) and the anisotropy index (b) obtained from the mean temperature model. The cross sections are taken at the center of the $\mathrm{y}-$ axis.

Acknowledgements

The provision of the computational resources are made possible through the ERC grant TRANSCALE: Reconciling Scales in Global Seismology project. All computations were carried out through the in-house Transcale cluster situated at the University of Lyon, France.

We are extremely grateful to editor Paula Koelemeijer, reviewer Manuele Faccenda, and one anonymous reviewer for their constructive feedback.

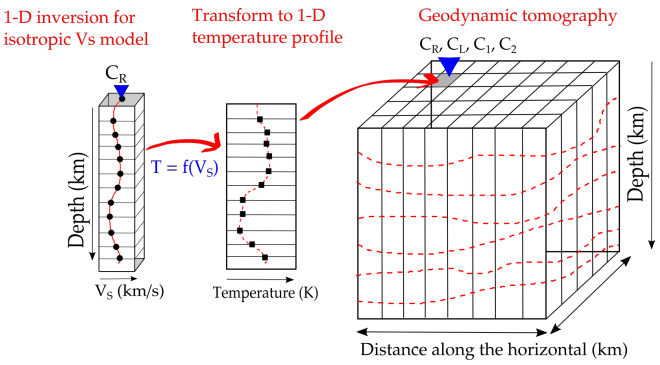

Figure 14 Three-step approach to geodynamic tomography. The first step involves 1-D isotropic surface wave tomography to infer the V_S structure (solid red lines) from a geographical array of isotropic Rayleigh wave dispersion measurements (blue triangle on top of the 1-D column). From the 1-D V_S structures, the second step is the estimation of 1-D temperature profiles (dashed red lines across the 1-D column). From the set of 1-D temperature profiles, one may then build a smooth 3-D model of temperature through interpolation. The 3-D model can thus be viewed as a collection of 1-D columns containing depth profiles of temperature. Geodynamic tomography commences by using the 3-D temperature field (dashed red lines in the 3-D model) as a starting model followed by its iterative update through the inversion of anisotropic surface wave dispersion measurements (blue triangles on top of the 3-D model).

Code and data availability statements

The codes used to generate the synthetic data and to demonstrate geodynamic tomography can be accessed freely at https://doi.org/10.5281/zenodo.6857279. This study purely worked on synthetics. No data have been used or produced in this work.

Competing interests

The authors declare no competing interests.

References

Afonso, J., Fullea, J., Yang, Y., Connolly, J., and Jones, A. 3-D multi-observable probabilistic inversion for the compositional and thermal structure of the lithosphere and upper mantle. II: General methodology and resolution analysis. *Journal of Geophysical Research: Solid Earth*, 118(4):1650–1676, 2013a. doi: https://doi.org/10.1002/jgrb.50123.

Afonso, J. C., Fullea, J., Griffin, W. L., Yang, Y., Jones, A. G., D. Connolly, J. A., and O'Reilly, S. Y. 3-D multiobservable probabilistic inversion for the compositional and thermal structure of the lithosphere and upper mantle. I: a priori petrological information and geophysical observables. *Journal of Geophysical Research: Solid Earth*, 118(5):2586–2617, 2013b. doi: https://doi.org/10.1002/jgrb.50124.

Babuska, V. and Cara, M. *Seismic anisotropy in the Earth*, volume 10. Springer Science & Business Media, 1991. doi: https://doi.org/10.1007/978-94-011-3600-6.

Baumann, T. and Kaus, B. J. Geodynamic inversion to constrain the non-linear rheology of the lithosphere. *Geophysical Journal International*, 202(2):1289–1316, 07 2015. doi: 10.1093/gji/ggv201.

Becker, T. W., Kellogg, J. B., Ekström, G., and O'Connell, R. J. Comparison of azimuthal seismic anisotropy from surface waves and finite strain from global mantle-circulation models. *Geophysical Journal International*, 155(2):696–714, 11 2003. doi: 10.1046/j.1365-246X.2003.02085.x.

Bercovici, D. On the purpose of toroidal motion in a convecting mantle. *Geophysical Research Letters*, 22(23):3107–3110, 1995. doi: https://doi.org/10.1029/95GL03082.

Billen, M. I. and Hirth, G. Newtonian versus non-Newtonian upper mantle viscosity: Implications for subduction initiation. *Geophysical Research Letters*, 32(19), 2005. doi: https://doi.org/10.1029/2005GL023457.

Bishop, C. M. et al. *Neural networks for pattern recognition*. Oxford university press, 1995.

Bissig, F., Khan, A., Tauzin, B., Sossi, P. A., Munch, F. D., and Giardini, D. Multifrequency Inversion of Ps and Sp Receiver Functions: Methodology and Application to USArray Data. *Journal of Geophysical Research: Solid Earth*, 126(2):e2020JB020350, 2021. doi: https://doi.org/10.1029/2020JB020350.

Chang, S.-J., Ferreira, A. M., and Faccenda, M. Upper-and mid-mantle interaction between the Samoan plume and the Tonga–Kermadec slabs. *Nature communications*, 7(1):1–9, 2016. doi: https://doi.org/10.1038/ncomms10799.

Christensen, U. Convection in a variable-viscosity fluid: Newtonian versus power-law rheology. *Earth and Planetary Science Letters*, 64(1):153–162, 1983. doi: https://doi.org/10.1016/0012-821X(83)90060-2.

Connolly, J. The geodynamic equation of state: what and how. *Geochemistry, Geophysics, Geosystems*, 10(10), 2009. doi: https://doi.org/10.1029/2009GC002540.

Connolly, J. A. Computation of phase equilibria by linear programming: a tool for geodynamic modeling and its application to subduction zone decarbonation. *Earth and Planetary Science Letters*, 236(1-2):524–541, 2005. doi: https://doi.org/10.1016/j.epsl.2005.04.033.

Conway, D., Alexander, B., King, M., Heinson, G., and Kee, Y. Inverting magnetotelluric responses in a three-dimensional earth using fast forward approximations based on artificial neural networks. *Computers & Geosciences*, 127:44–52, 2019. doi: https://doi.org/10.1016/j.cageo.2019.03.002.

Debayle, E. and Kennett, B. Anisotropy in the Australasian upper mantle from Love and Rayleigh waveform inversion. *Earth and Planetary Science Letters*, 184(1):339–351, 2000. doi: https://doi.org/10.1016/S0012-821X(00)00314-9.

Faccenda, M. Mid mantle seismic anisotropy around subduction zones. *Physics of the Earth and Planetary Interiors*, 227:1–19, 2014. doi: https://doi.org/10.1016/j.pepi.2013.11.015.

Faccenda, M. and Capitanio, F. A. Development of mantle seismic anisotropy during subduction-induced 3-D flow. *Geophysical Research Letters*, 39(11), 2012. doi: https://doi.org/10.1029/2012GL051988.

Faccenda, M. and Capitanio, F. A. Seismic anisotropy around subduction zones: Insights from three-dimensional modeling of upper mantle deformation and SKS splitting calculations. *Geochemistry, Geophysics, Geosystems*, 14(1):243–262, 2013. doi: https://doi.org/10.1002/ggge.20055.

Fukao, Y., Obayashi, M., and Nakakuki, T. a. Stagnant Slab: A Review. *Annual Review of Earth and Planetary Sciences*, 37(1): 19–46, 2009. doi: 10.1146/annurev.earth.36.031207.124224.

Gable, C. W., O'connell, R. J., and Travis, B. J. Convection in three dimensions with surface plates: Generation of toroidal flow.

Journal of Geophysical Research: Solid Earth, 96(B5):8391–8405, 1991. doi: https://doi.org/10.1029/90JB02743.

Hansen, T. M. and Cordua, K. S. Efficient Monte Carlo sampling of inverse problems using a neural network-based forward—applied to GPR crosshole traveltime inversion. *Geophysical Journal International*, 211(3):1524–1533, 2017. doi: https://doi.org/10.1093/gji/ggx380.

Hirth, G. and Kohlstedf, D. Rheology of the upper mantle and the mantle wedge: A view from the experimentalists. *Geophysical monograph-american geophysical union*, 138:83–106, 2003. doi: https://doi.org/10.1029/138GM06.

Kaminski, E. and Ribe, N. M. Timescales for the evolution of seismic anisotropy in mantle flow. *Geochemistry, Geophysics, Geosystems*, 3(8):1–17, 2002. doi: https://doi.org/10.1029/2001GC000222.

Kaminski, E., Ribe, N. M., and Browaeys, J. T. D-Rex, a program for calculation of seismic anisotropy due to crystal lattice preferred orientation in the convective upper mantle. *Geophysical Journal International*, 158(2):744–752, 2004. doi: https://doi.org/10.1111/j.1365-246X.2004.02308.x.

Karato, S. and Wu, P. Rheology of the upper mantle: A synthesis. *Science*, 260(5109):771–778, 1993. doi: https://doi.org/10.1126/science.260.5109.771.

Köpke, C., Irving, J., and Elsheikh, A. H. Accounting for model error in Bayesian solutions to hydrogeophysical inverse problems using a local basis approach. *Advances in water resources*, 116:195–207, 2018. doi: https://doi.org/10.1016/j.advwatres.2017.11.013.

LeCun, Y., Bengio, Y., and Hinton, G. Deep learning. *nature*, 521 (7553):436, 2015. doi: https://doi.org/10.1038/nature14539.

Long, M. D. and Becker, T. W. Mantle dynamics and seismic anisotropy. *Earth and Planetary Science Letters*, 297(3-4): 341–354, 2010. doi: https://doi.org/10.1016/j.epsl.2010.06.036.

Love, A. A Treaties on the Mathematical Theory of Elasticity. *A treaties on the Mathematical Theory of Elasticity*, 643, 1927.

MacDougall, J. G., Jadamec, M. A., and Fischer, K. M. The zone of influence of the subducting slab in the asthenospheric mantle. *Journal of Geophysical Research: Solid Earth*, 122(8):6599–6624, 2017. doi: https://doi.org/10.1002/2017JB014445.

Magali, J., Bodin, T., Hedjazian, N., Ricard, Y., Capdeville, Y., and Debayle, E. Quantifying intrinsic and extrinsic contributions to radial anisotropy in tomographic models. *Journal of Geophysical Research: Solid Earth*, 126(10):e2021JB022322, 2021a. doi: https://doi.org/10.1029/2021JB022322.

Magali, J. K. *Geodynamic Tomography*. PhD thesis, Université de Lyon, 2021.

Magali, J. K., Bodin, T., Hedjazian, N., Samuel, H., and Atkins, S. Geodynamic tomography: constraining upper-mantle deformation patterns from Bayesian inversion of surface waves. *Geophysical Journal International*, 224(3):2077–2099, 2021b. doi: https://doi.org/10.1093/gji/ggaa577.

Maupin, V. and Park, J. 1.09—Theory and observations—Seismic anisotropy. *Treatise on Geophysics*, pages 277–305, 2015. doi: https://doi.org/10.1016/B978-0-444-53802-4.00007-5.

Moghadas, D., Behroozmand, A. A., and Christiansen, A. V. Soil electrical conductivity imaging using a neural network-based forward solver: Applied to large-scale Bayesian electromagnetic inversion. *Journal of Applied Geophysics*, page 104012, 2020. doi: https://doi.org/10.1016/j.jappgeo.2020.104012.

Montagner, J.-P. and Jobert, N. Vectorial tomography—ii. Application to the Indian Ocean. *Geophysical Journal International*, 94(2):309–344, 1988. doi: https://doi.org/10.1111/j.1365-246X.1988.tb05904.x.

Montagner, J.-P. and Nataf, H.-C. A simple method for inverting the azimuthal anisotropy of surface waves. *Journal of Geophysical Research: Solid Earth*, 91(B1):511–520, 1986. doi: https://doi.org/10.1029/JB091iB01p00511.

Montagner, J.-P. and Nataf, H.-C. Vectorial tomography—I. Theory. *Geophysical Journal International*, 94(2):295–307, 1988. doi: https://doi.org/10.1111/j.1365-246X.1988.tb05903.x.

Montagner, J.-P. and Tanimoto, T. Global upper mantle tomography of seismic velocities and anisotropies. *Journal of Geophysical Research: Solid Earth*, 96(B12):20337–20351, 1991. doi: https://doi.org/10.1029/91JB01890.

Nakanishi, I. and Anderson, D. L. Measurement of mantle wave velocities and inversion for lateral heterogeneity and anisotropy: 1. Analysis of great circle phase velocities. *Journal of Geophysical Research: Solid Earth*, 88(B12):10267–10283, 1983. doi: https://doi.org/10.1111/j.1365-246X.1984.tb01964.x.

Obrebski, M., Kiselev, S., Vinnik, L., and Montagner, J.-P. Anisotropic stratification beneath Africa from joint inversion of SKS and P receiver functions. *Journal of Geophysical Research: Solid Earth*, 115(B9), 2010. doi: https://doi.org/10.1029/2009JB006923.

Obrebski, M., Allen, R. M., Pollitz, F., and Hung, S.-H. Lithosphere–asthenosphere interaction beneath the western United States from the joint inversion of body-wave traveltimes and surface-wave phase velocities. *Geophysical Journal International*, 185(2):1003–1021, 2011. doi: https://doi.org/10.1111/j.1365-246X.2011.04990.x.

OpenMP Architecture Review Board. OpenMP Application Program Interface Version 3.0, May 2008.

Panning, M. and Romanowicz, B. A three-dimensional radially anisotropic model of shear velocity in the whole mantle. *Geophysical Journal International*, 167(1):361–379, 2006. doi: https://doi.org/10.1111/j.1365-246X.2006.03100.x.

Piromallo, C., Becker, T., Funiciello, F., and Faccenna, C. Three-dimensional instantaneous mantle flow induced by subduction. *Geophysical Research Letters*, 33(8), 2006. doi: https://doi.org/10.1029/2005GL025390.

Romanowicz, B. Inversion of surface waves: a review. *International Geophysics Series*, 81(A):149–174, 2002.

Saito, M. DISPER80: A subroutine package for the calculation of seismic normal-mode solutions. *Seismological algorithms*, pages 293–319, 1988.

Samuel, H. Time domain parallelization for computational geodynamics. *Geochemistry, Geophysics, Geosystems*, 13(1), 2012. doi: https://doi.org/10.1029/2011GC003905.

Samuel, H. A Deformable Particle-In-Cell Method for Advective Transport in Geodynamic Modelling. *gji*, 214: 1744–1773, 2018. doi: https://doi.org/10.1093/gji/ggy231. doi:10.1093/gji/ggy231.

Smith, M. L. and Dahlen, F. The azimuthal dependence of Love and Rayleigh wave propagation in a slightly anisotropic medium. *Journal of Geophysical Research*, 78(17):3321–3333, 1973. doi: https://doi.org/10.1029/JB078i017p03321.

Stixrude, L. and Lithgow-Bertelloni, C. Thermodynamics of mantle minerals-II. Phase equilibria. *Geophysical Journal International*, 184(3):1180–1213, 2011. doi: https://doi.org/10.1111/j.1365-246X.2010.04890.x.

Xie, J., Ritzwoller, M. H., Brownlee, S., and Hacker, B. Inferring the oriented elastic tensor from surface wave observations: preliminary application across the western United States. *Geophysical Journal International*, 201(2):996–1021, 2015. doi: https://doi.org/10.1093/gji/ggv054.

Xie, J., Ritzwoller, M. H., Shen, W., and Wang, W. Crustal anisotropy

across eastern Tibet and surroundings modeled as a depth-dependent tilted hexagonally symmetric medium. *Geophysical Journal International*, 209(1):466–491, 2017. doi: https://-doi.org/10.1093/gji/ggx004.